Fluorescence color tuning of dual-emission carbon quantum dots produced from biomass and their use in Fe^{3+} and Cu^{2+} detection

XUE Jia-jia, GAN Mei-heng, LU Yong-gen, WU Qi-lin*

（*State Key Laboratory for Modification of Chemical Fibers and Polymer Materials*, *College of Materials Science and Engineering*, *Donghua University*, *Shanghai* 201620, *China*）

Abstract: Using simple and eco-friendly ethanol solvothermal treatment, **dual-emission** biomass carbon quantum dots (D-BCQDs) were synthesized from biomass viburnum awabuki leaves. Under excitation with 413 nm wavelength light two emission peaks appeared at 490 and 675 nm and the dots could be tuned to emit crimson, red, purplish red, purple and blue-gray fluorescence by changing the solvothermal temperature from 140 °C to 160, 180, 200 and 240 °C, respectively. XPS and FTIR characterization indicated that the fluorescence color was mainly determined by surface oxidation defects, elemental nitrogen and sp^2-C/sp^3-C hybridized structural domains. The D-BCQDs could not only detect Fe^{3+} or Cu^{2+}, but also quantify the concentration ratio of Fe^{3+} to Cu^{2+} in a solution containing both, demonstrating their potential applications in the simultaneous detection of Fe^{3+} and Cu^{2+} ions.

Key words: Dual-emission biomass carbon quantum dots; Multicolor; Solvothermal method; Ion detection

1 Introduction

CQDs (carbon quantum dots) are emerging as an alternative to conventional semiconductor quantum dots and organic fluorescent dyes due to their exceptional photostability, low toxicity, biocompatibility and small size[1,2]. These characteristics make CQDs highly promising for a wide range of applications, including metal ion sensing[3], bioimaging[4,5], drug delivery[6] and photocatalysis[7]. BCQDs prepared from natural biomass have excellent biocompatibility and fluorescence properties[8]. However, most BCQDs emit blue-green fluorescence, which limits their applications in fluorescence sensing[9-11]. Consequently, there is an urgent need to synthesize long-wavelength emission or multicolor BCQDs.

In nature, plant leaves naturally contain chlorophyll with a porphyrin structure, which exhibits strong near-infrared absorption and emission properties. This intrinsic characteristic renders them highly suitable for synthesizing long-wavelength BCQDs. For instance, Qu et al.[12] synthesized near-infrared light BCQDs from magnolia leaves and applied them to the detection of Pd^{2+}. In addition, researchers have synthesized long-wavelength red BCQDs using taxus[13] and mulberry leaves[14] as carbon sources.

Currently, three luminescence mechanisms have been identified and accepted: the quantum confinement effect[15], surface state luminescence (involving surface chemical groups, surface oxidation degree and surface defects[16]) and molecular state luminescence[17]. Consequently, researchers modify the particle size and surface state of BCQDs by precisely controlling reaction conditions, including reaction temperature, time, solvent and precursors[18]. Additionally, heteroatom doping is implemented further to enhance the tunability and multicolor luminescence of BCQDs. However, the tunable fluorescence color mechanism of multicolor **dual-emission BCQDs (D-BCQDs)** has rarely been studied.

Excessive intake of Fe^{3+} and Cu^{2+} is known to cause severe harm to humans[19,20]. Therefore, detecting heavy metal ions including Fe^{3+} and Cu^{2+} is essential for protecting human health and ecological environment. Currently, most fluorescent probes used for detecting metal ions rely on single-emission fluorescence analysis, and are susceptible to interference from factors like probe concentration and environmental conditions, which may hamper the accurate analysis of the target analytes[21]. In contrast, dual-

Received date: 2023-11-07; **Revised date:** 2024-01-19

Corresponding author: WU Qi-lin, Professor. E-mail: wql@dhu.edu.cn

Author introduction: XUE Jia-jia, Master student. E-mail: xuejiajia654321@163.com

emission CQDs can establish a relationship to the content of the target based on the change in the ratio of the two emission peaks, which is conducive to eliminating some of the disadvantages mentioned above and improves the accuracy and sensitivity of detection[22]. Moreover, fluorescence color changes of **D-BCQDs** are easy to be recognized by naked eyes. Therefore, it is of interest to develop a simple method for preparing D-BCQDs to detect Fe^{3+} and Cu^{2+}.

We used *Viburnum awabuki* leaves as raw materials to prepare D-BCQDs by a one-step solvothermal method. The resulting D-BCQDs exhibited a blue fluorescence peak at 490 nm and a red fluorescence peak at 675 nm under the excitation wavelength of 413 nm. Multicolor D-BCQDs from blue to red were synthesized by adjusting reaction temperatures, achieving controllable regulation of D-BCQDs fluorescence color. Notably, we used ethanol as the only solvent, which minimized environmental pollution and realized green and sustainable development. Additionally, the mechanism of the tunable fluorescence color of D-BCQDs was investigated and its selectivity and sensitivity for detecting metal ions were analyzed.

2 Experimental

2.1 Materials and reagents

Viburnum awabuki leaves were harvested from the campus of Donghua University (Shanghai, China). Ethanol was supplied by Shanghai Titan Technology Co. Deionized water was produced in-house by the laboratory. Iron (Ⅲ) chloride hexahydrate ($FeCl_3·6H_2O$), copper (Ⅱ) chloride dihydrate ($CuCl_2·2H_2O$), chromium chloride hexahydrate ($CrCl_3·6H_2O$), cobalt chloride hexahydrate ($CoCl_2·6H_2O$), calcium chloride ($CaCl_2$), zinc chloride ($ZnCl_2$), magnesium chloride hexahydrate ($MgCl_2·6H_2O$), aluminum chloride hexahydrate ($AlCl_3·6H_2O$), manganese (Ⅱ) chloride ($MnCl_2$) and nickel (Ⅱ) chloride hexahydrate ($NiCl_2·6H_2O$) were sourced from Sinopharm Chemical Reagent Co. Ltd. All the aforementioned reagents are of analytical grade and were used directly without further purification.

2.2 Synthesis of multicolor D-BCQDs

Multicolor D-BCQDs were synthesized using *Viburnum awabuki* leaves as the carbon source and ethanol solution as solvent by a one-step solvothermal process (Fig. 1). Initially, fresh leaves were meticulously cleaned with deionized water, dried at 75 °C for 4 h, and subsequently ground into fine powder. After 0.2 g of the powder was mixed with 30 mL of ethanol solution for 5 min at room temperature, the mixture was put into a 100 mL Teflon-lined stainless steel autoclave. The autoclave was then sealed and heated for 6 h at different temperatures (140, 160, 180, 200

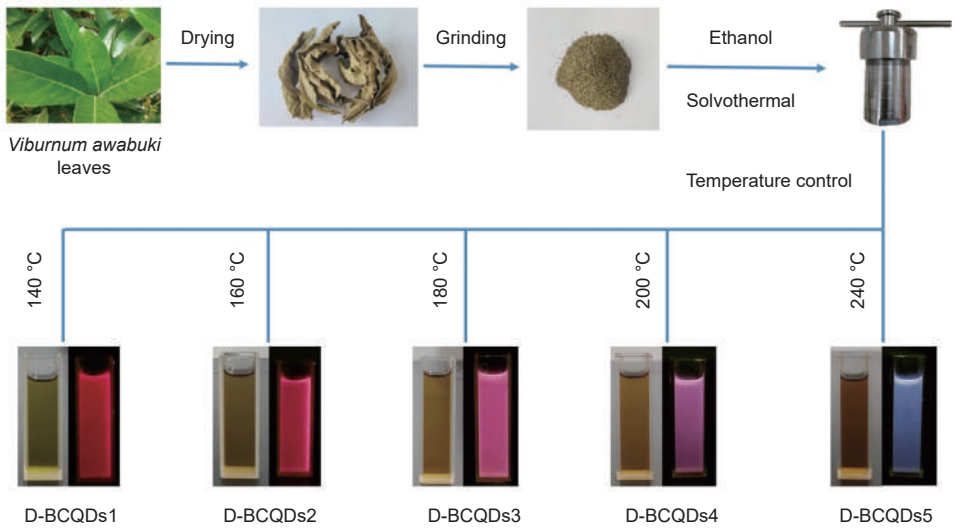

Fig. 1 Schematic illustration of the synthesis of multicolor D-BCQDs (insets: the photographs of D-BCQD solutions under daylight (left) and 365 nm UV light (right))

and 240 °C). After cooling down to room temperature, the crude product solution was filtered using a 0.22 μm filter membrane and subsequently purified via a dialysis bag with 1 000 molecular weight cut-off (MW:1000D) for 48 h. The resulting solution was stored in centrifuge tubes, pre-treated by freezing with liquid nitrogen and subsequently subjected to vacuum drying in a freeze dryer for 3 days. The powder of the D-BCQDs was obtained and stored in a refrigerator at 4 °C for further characterization and application. The five D-BCQDs obtained at 140, 160, 180, 200 and 240 °C were named D-BCQDs1 (crimson), D-BCQDs2 (red), D-BCQDs3 (purplish red), D-BCQDs4 (purple) and D-BCQDs5 (blue-gray), respectively.

2.3 Characterization

Transmission electron microscopy (TEM, JEM-2100, Japan) was used to analyze the morphology, particle size and crystal spacing of D-BCQDs. Fourier transform infrared spectroscopy (FTIR, Nicolet is50, USA) was used to characterize the composition and structure of D-BCQDs. X-ray photoelectron spectroscopy (XPS, Escalab250Xi, China) was used to analyze the elemental composition and content of D-BCQDs. Fluorescence spectra of D-BCQDs were recorded by a steady-state/transient fluorescence emission spectrometer (FLS920 Edinburgh, Scotland). The UV-Vis absorption spectra of D-BCQDs were recorded by a UV-Vis spectrophotometer (LanbdaA35, USA). The XRD patterns of D-BCQDs were determined using a Powder X-ray diffractometer (XRD; Bruker D8 Advance, Germany).

2.4 Detection of Fe^{3+} and Cu^{2+}

2.4.1 Selectivity of D-BCQDs

Ten ethanol solutions of metal ions (Fe^{3+}, Cu^{2+}, Cr^{3+}, Co^{2+}, Ca^{2+}, Zn^{2+}, Mg^{2+}, Al^{3+}, Mn^{2+}, Ni^{2+}) were prepared at room temperature with a concentration of 2 mmol L^{-1}. Subsequently, 2 mL of each metal ion solution was added to 2 mL of D-BCQDs3 solution (1.11 mg/mL) to evaluate the selectivity for Fe^{3+} and Cu^{2+}. The fluorescence emission spectra of the mixed solutions at 360 nm excitation wavelength were recorded.

2.4.2 Detection of Fe^{3+} and Cu^{2+}at different concentrations

D-BCQDs3 solution (1.11 mg/mL) was mixed with different volumes of Fe^{3+} solution to get final Fe^{3+} concentrations ranging from 0 to 0.2 mmol L^{-1}. Then, the fluorescence emission spectra of the mixed solutions at 360 nm excitation wavelength were collected to assess the sensitivity towards Fe^{3+}. The same experimental procedure was applied to detect Cu^{2+}, with final Cu^{2+} concentrations ranging from 0 to 0.22 mmol L^{-1}.

To verify the anti-interference ability of D-BCQDs3, the D-BCQDs3 solution was mixed with Fe^{3+} or Cu^{2+} at a concentration ratio of 1∶1. The fluorescence emission intensity at 490 and 675 nm wavelengths with and without other interfering metal ions were measured and analyzed.

3 Results and discussion

3.1 Optical properties of D-BCQDs

According to the UV-vis absorption, excitation, and emission spectra as shown in Fig. 2, D-BCQDs exhibited 4 distinct absorption bands. The absorption peaks observed at around 210 and 270 nm were caused by the π-π* transition of C＝C[23], while the absorption peaks at 410 and 665 nm could be attributed to the n-π* transition of C＝O in the chlorophyll-derived porphyrin structure[24]. Moreover, as shown in Fig. 2f, the absorption peaks at 410 and 665 nm gradually diminished when the reaction temperature increased, and the absorption peak at 665 nm vanished at 240 °C, indicating that the porphyrin structure may have been completely carbonized[25].

The optimal excitation wavelength for D-BCQDs was determined to be 413 nm (Fig. 2). Under this excitation wavelength, five D-BCQDs had 2 distinct fluorescence emission peaks. The first emission peak was observed at 490 nm, corresponding to the blue-green emission band, while the second emission peak was observed at 675 nm, corresponding to the red emission band. Thus, the synthesized D-BCQDs displayed a unique fluorescence emission behavior characterized by a single excitation wavelength and dual

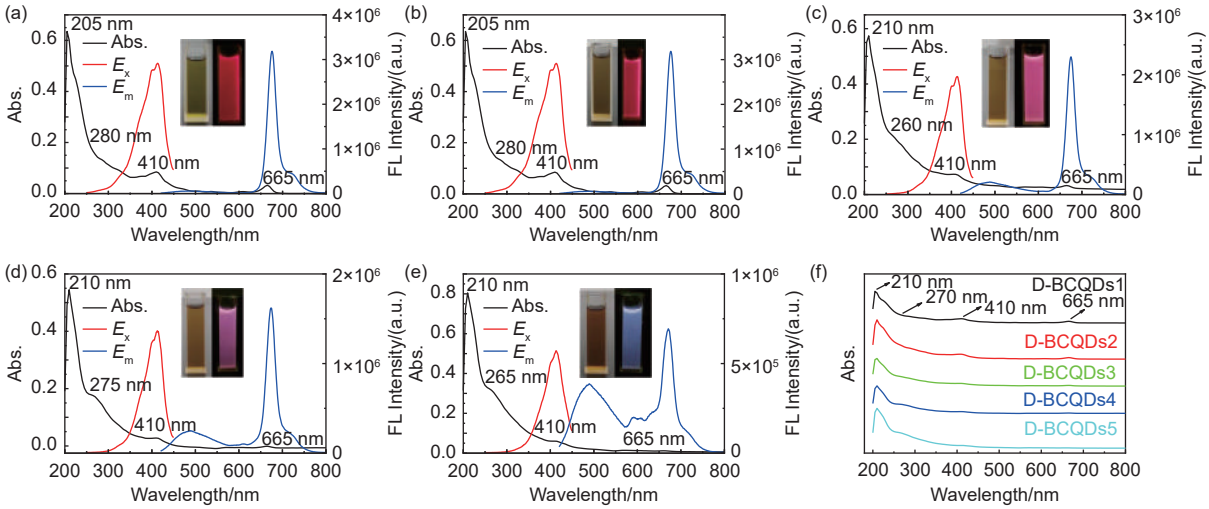

Fig. 2 UV-Vis absorption, excitation and emission spectra of (a) D-BCQDs1, (b) D-BCQDs2, (c) D-BCQDs3, (d) D-BCQDs4 and (e) D-BCQDs5. (f) Comparison of UV-Vis absorption spectra of D-BCQDs

emission peaks. As reported in the literatures, the two peaks of dual-emission CQDs can be in the blue and red emission bands[26,27], which were typically found in most plant leaves[28], like D-BCQDs prepared in this work. Alternatively, the peaks can be in the blue and yellow[29,30], or the blue and green emission bands[31-33]. However, it was discovered that the variation in the distance between the 2 emission peaks could be mainly related to carbon source precursors and reaction conditions.

When illuminated with UV light at 365 nm, the D-BCQDs1, 2, 3, 4 and 5 emitted diverse fluorescent colors including crimson, red, purplish red, purple, and blue-gray, respectively (Fig. 2). The corresponding quantum yields of D-BCQDs were measured to be 12.49%, 10.72%, 16.68%, 9.57% and 7.02%, respectively. As a result, the synthesis of multicolor D-BCQDs was achieved by only manipulating the reaction temperature.

The fluorescence emission spectra of D-BCQDs at various excitation wavelengths were shown in Fig. 3a-e. As the excitation wavelength increased from 340 to 540 nm, it was noticed that the emission of the blue fluorescence band (Peak 1) experienced a red shift and displayed excitation-dependent properties (Fig. 3f). Previous studies suggested that this phe-

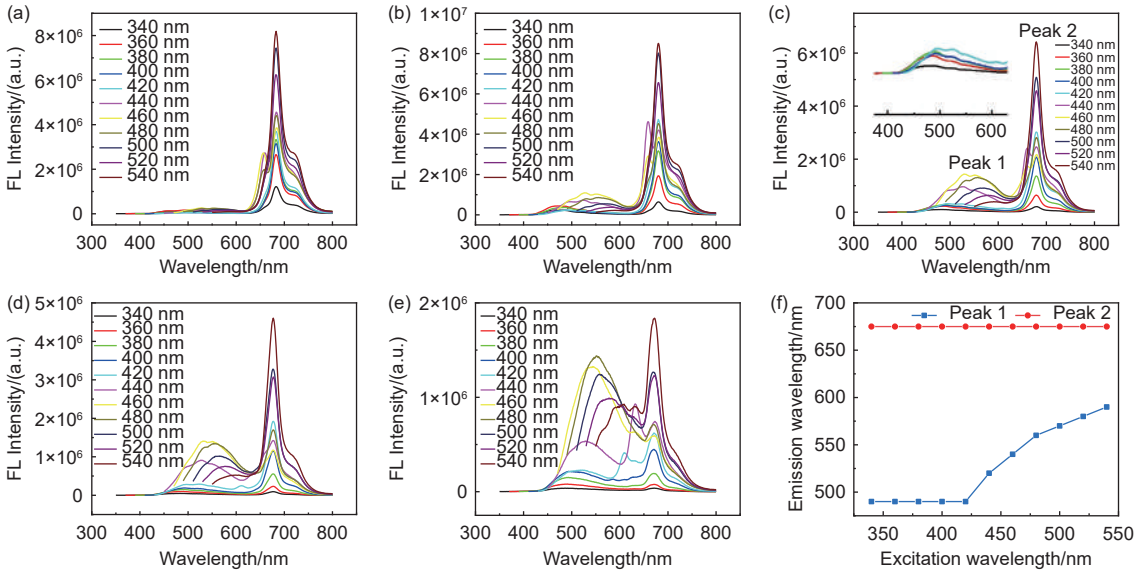

Fig. 3 Fluorescence emission spectra at different excitation wavelengths: (a) D-BCQDs1, (b) D-BCQDs2, (c) D-BCQDs3, (d) D-BCQDs4 and (e) D-BCQDs5. (f) The influence of excitation wavelength on emission wavelength (D-BCQDs3 as an example)

nomenon can be attributed to intrinsic and defect emissions, which were associated with oxygen-related defect states. In contrast, the emission of the red fluorescence band (Peak 2) displayed excitation-independent behavior, where the fluorescence emission wavelength remained constant and only the fluorescence emission intensity varied. Porphyrin molecules and other nitrogen-containing organic fluorophores can be responsible for this behavior[34-36].

3.2 Morphology and microstructure of D-BCQDs

TEM images of D-BCQDs1, D-BCQDs3 and D-BCQDs5 were shown in Fig. 4a, b and c, respectively. All the particles of D-BCQDs1, D-BCQDs3 and D-BCQDs5 were quasi-spherical and well-dispersed with a uniform size distribution of average sizes of 3.57 ± 0.57, 3.97 ± 0.97 and 3.66 ± 0.48 nm, respectively (the inset of Fig. 4a-c). The HR-TEM images of the D-BCQDs1, D-BCQDs3 and D-BCQDs5 showed well-resolved lattice stripes with lattice spacings of 0.208, 0.212 and 0.214 nm, respectively, corresponding to the (100) plane of graphite[32]. The differences in particle sizes among the D-BCQDs were not significant, indicating that the quantum size effect was not the main reason affecting the fluorescence color of D-BCQDs[37]. As shown in Fig. 4d, there was an obvious broad diffraction peak at $2\theta \approx 20°$ corresponding to the (002) crystal planes of graphite, indicating the amorphous nature of D-BCQDs[38].

The structure and elemental composition of the D-BCQDs were analyzed by FT-IR and XPS. The detailed results were displayed in Fig. 5. Five D-BCQDs demonstrated similar absorption peaks (Fig. 5a). The broad absorption peak around 3 380 cm^{-1} was attributed to the stretching vibrations of O—H and N—H, while the absorption peak near 2 920 cm^{-1} corresponded to the stretching vibration of C—H[39]. It was

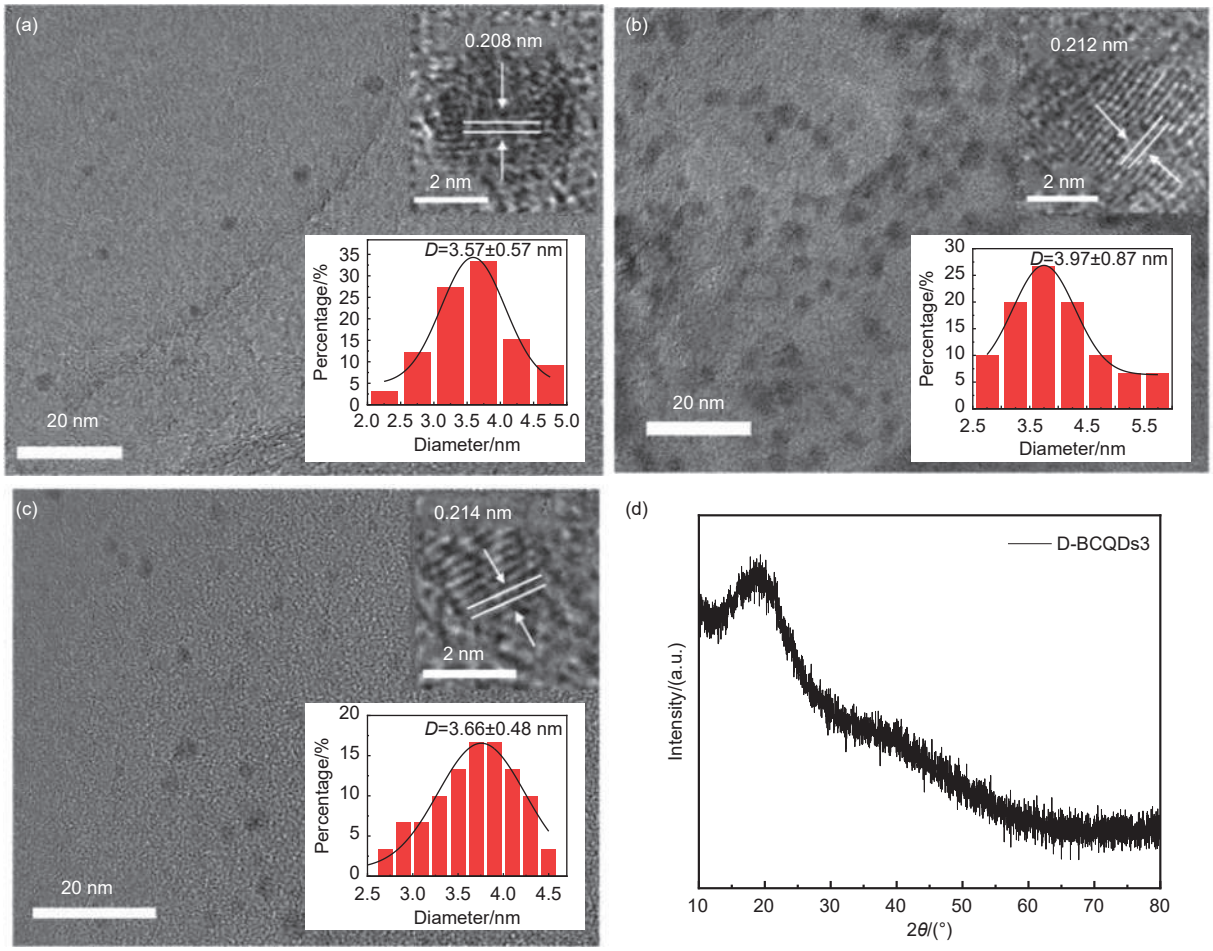

Fig. 4　TEM images of (a) D-BCQDs1, (b) D-BCQDs3 and (c) D-BCQDs5 (insets: the corresponding particle size distributions). (d) XRD pattern of D-BCQDs3

proved that D-BCQDs contained abundant functional groups such as —OH, —COOH, —NH, suggesting the existence of porphyrin structures[34]. The characteristic absorption peaks near 1 720, 1 590 and 1 080 cm^{-1} can be assigned to C=O, C=C and C—O stretching vibrations[40], suggesting that the D-BCQDs contained sp^2-C/sp^3-C hybridized structures[41]. It was noteworthy that the intensity of C—O stretching vibration at 1 080 cm^{-1} gradually increased and the C=C at 1 590 cm^{-1} gradually weakened with increasing the reaction temperature in preparation of D-BCQDs.

The XPS spectra in Fig. 5b revealed all spectra had peaks at 285, 400 and 532 eV, indicating these D-BCQDs mainly consisted of C, N and O. The high-resolution XPS spectra of C1s, N1s and O1s were presented in Fig. 6, revealing that 5 D-BCQDs possessed similar chemical bonding species. The C1s spectra can be divided into 4 peaks at 284, 285.1, 286.5 and 288.3 eV, corresponding to C=C (sp^2-C), C—C (sp^3-C), C—O and C=O, respectively. Similarly, the N1s spectra can be resolved into 2 peaks at 399.7 and 400.6 eV, related to pyridinic N and pyrrolic N, respectively[42]. The O1s spectra had two peaks at 532.1 and 533 eV, attributed to C=O and C—O, respectively[43]. It was observed that the relative content of pyridinic nitrogen displayed a decreasing trend, which affected the N content in D-BCQDs[44]. The contents of sp^2-C and sp^3-C hybridization domains were obtained by calculating the area of the fitted curves (Table 1).

3.3 Fluorescence tunable mechanism

To clarify the mechanism of the reaction temperature-based tuning of fluorescence colors, we compared the fluorescence emission intensities of the synthesized D-BCQDs. It was found that the blue fluorescence peak at 490 nm gradually strengthened, while the red fluorescence peak at 675 nm steadily weakened with the increase of reaction temperature (Fig. 7a). Interestingly, the fluorescence intensity ratios of the 2 peaks were different (Fig. 7b). Furthermore, the oxygen elemental content steadily increased, while the nitrogen elemental content declined based on XPS elemental content analysis (Fig. 7c, d). As mentioned above, the source at 490 nm might be related to the oxygen-related defective states, while the emission at 675 nm originated from the nitrogen-containing fluorophores. Therefore, we speculated that the increase in blue fluorescence peaks at 490 nm from D-BCQDs1 to D-BCQDs5 was closely related to oxygen-related surface defect sites[45]. In contrast, the decline in the red fluorescence peak at 675 nm was mainly attributed to the reduction in the nitrogen elemental content.

It was reported that yellow and red emissions were associated with sp^2-C hybridization domains, while blue and green emissions were linked to sp^3-C hybridization domains. Multicolor CQDs might be synthesized by adjusting the ratio of hybridized domains by adjusting the reaction conditions[46]. Table 1 showed that the content of sp^2-C hybridized domains gradually reduced, while the sp^3-C steadily increased from D-BCQDs1 to D-BCQDs5. Furthermore, there was a decline in the ratio of sp^2-C to sp^3-C hybridized domains, which corresponded to the earlier observed changes in blue and red fluorescence intensity.

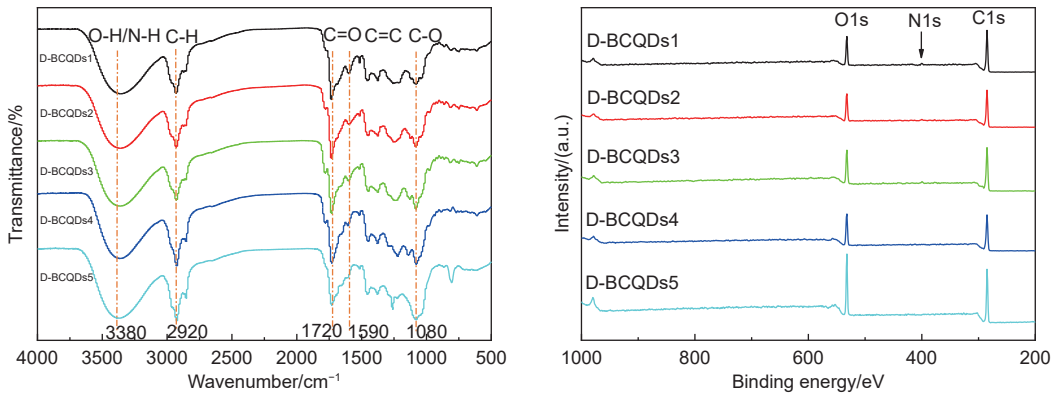

Fig. 5 (a) FT-IR and (b) XPS spectra of D-BCQDs

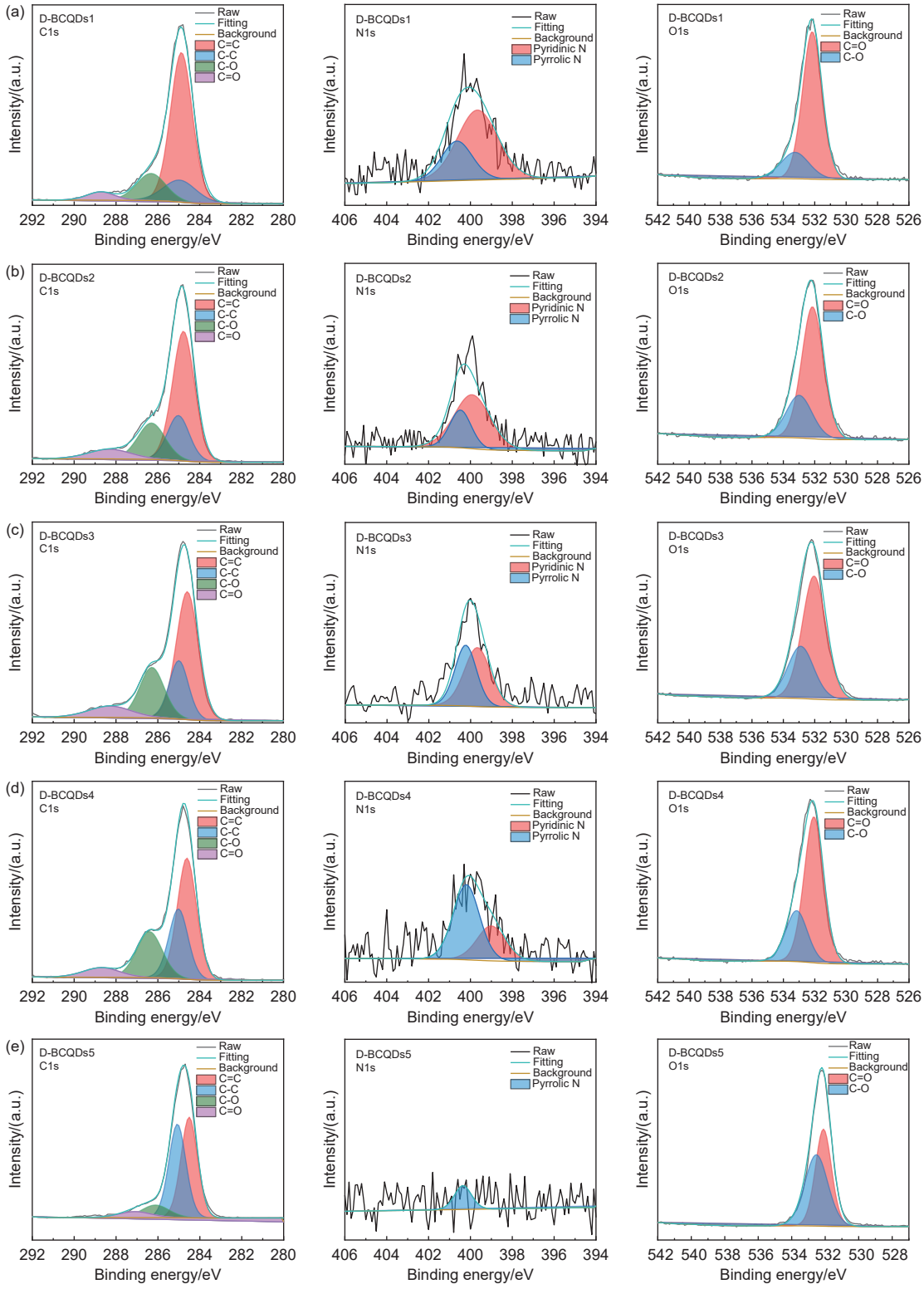

Fig. 6　High-resolution XPS spectra of (a) D-BCQDs1, (b) D-BCQDs2, (c) D-BCQDs3, (d) D-BCQDs4 and (e) D-BCQDs5

Table 1　Atomic percentages of sp^2-C and sp^3-C hybridization domains of multicolor D-BCQDs

Samples	sp^2-C/%	sp^3-C/%	sp^2-C/sp^3-C
D-BCQDs1	76.13	13.32	5.72
D-BCQDs2	69.81	19.65	3.55
D-BCQDs3	54.39	20.93	2.60
D-BCQDs4	53.70	20.73	2.59
D-BCQDs5	48.68	40.01	1.22

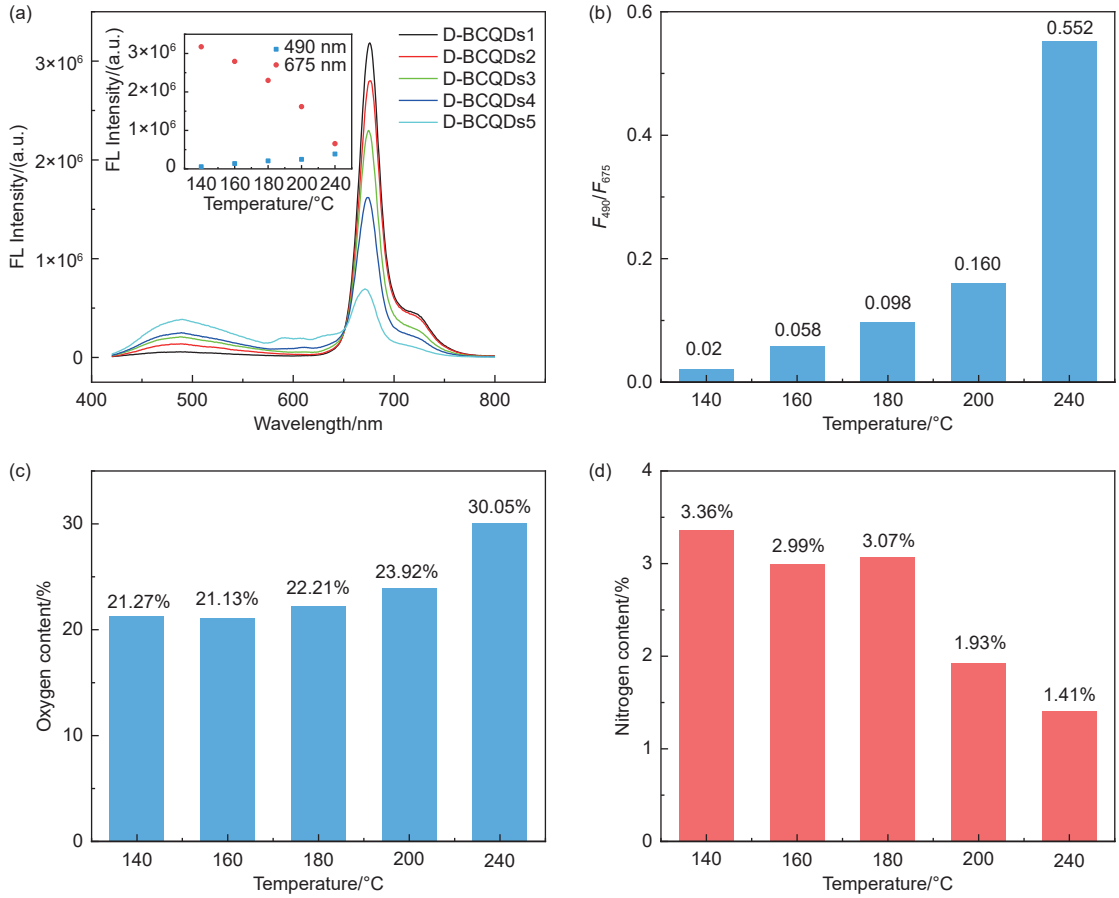

Fig. 7 (a) Fluorescence spectra of D-BCQDs at 413 nm excitation wavelength (inset: scatter plot of fluorescence intensities at 490 nm and 675 nm with the change of temperature). (b) The F_{490}/F_{675} intensity ratios of D-BCQDs at 413 nm excitation wavelength. (c) Oxygen contents of D-BCQDs. (d) Nitrogen contents of D-BCQDs

4 Application of D-BCQDs

4.1 Fe^{3+} and Cu^{2+} detection

D-BCQDs3 was selected as a fluorescent nanoprobe for detecting various metal ions. As shown in Fig. 8a, when Fe^{3+} was added to the D-BCQDs3 solution, it can be observed that purplish red fluorescence was almost completely quenched. In addition, the purplish red fluorescence turned into blue upon adding Cu^{2+}. However, other metal ions do not greatly affect the fluorescence color of D-BCQDs3 solutions. The changes in fluorescence intensity and fluorescence color were basically the same, which indicated that D-BCQDs3 had excellent selectivity for Fe^{3+} and Cu^{2+} detection.

The sensitivity of D-BCQDs3 for detecting Fe^{3+} and Cu^{2+} was further investigated. With the addition of Fe^{3+}, the fluorescence intensity of D-BCQDs3 at 490 and 675 nm gradually reduced (Fig. 9a). Meanwhile, the inset of Fig. 9a visually illustrated the purplish red fluorescence gradually quenched in a clockwise direction as the Fe^{3+} concentration increased. There was a good linear relationship between F_{675}/F_0 and Fe^{3+} concentration (R^2 = 0.996) in concentrations ranging from 0.02 to 0.2 mmol L^{-1} (Fig. 9b). The associated linear equation was F_{675}/F_0 = −4.83084C (mmol L^{-1}) + 0.97532, where F_0 represents the fluorescence intensity at 675 nm of D-BCQDs3 without Fe^{3+}, F_{675} indicates the fluorescence intensity at 675 nm after adding Fe^{3+}.

The limit of detection (LOD) for Fe^{3+} was calculated to be 0.592 μmol L^{-1} using the following equation:

$$\mathrm{LOD} = 3\delta/S \quad (1)$$

where δ denotes the standard deviation of the fluorescence intensity of D-BCQDs3 without Fe^{3+} (n=11, 11 measurements), and S is the slope of the linear equation curve[47].

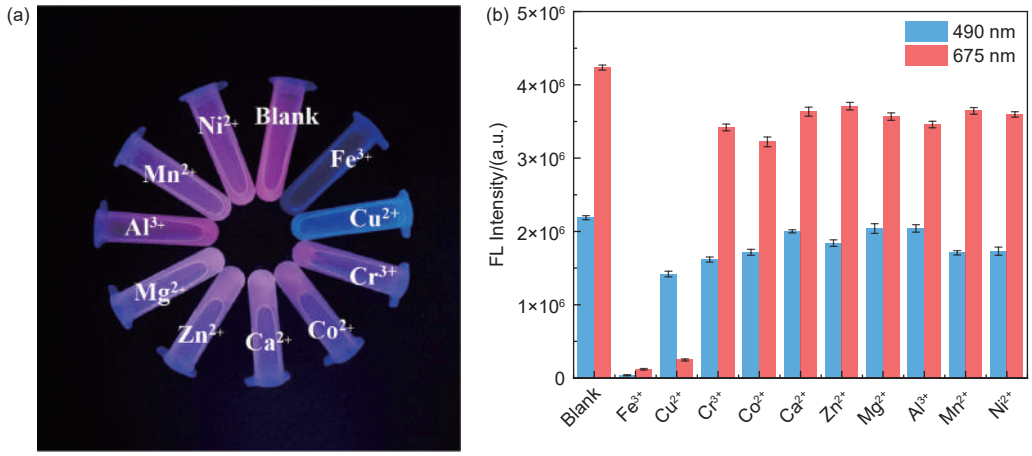

Fig. 8　(a) Fluorescence photographs of D-BCQDs3 after adding different metal ions under 365 nm UV light. (b) The changes of fluorescence intensity of D-BCQDs3 after adding different metal ions

As can be seen in Fig. 9c, the fluorescence intensity at 675 nm declined with increasing Cu^{2+} concentration, and there was a slight blueshift and decrease in fluorescence intensity at 490 nm. Consequently, the final color was blue under 365 nm UV light (the inset of Fig. 9c). Fig. 9d showed the relationship between F_{490}/F_{675} and Cu^{2+} concentration, and the linear equation in the range of 0.1–0.22 mmol L^{-1} was F_{490}/F_{675} = 7.07094C (mmol L^{-1}) − 0.04962, R^2 = 0.997. The LOD was 0.405 μmol L^{-1}. It was worth

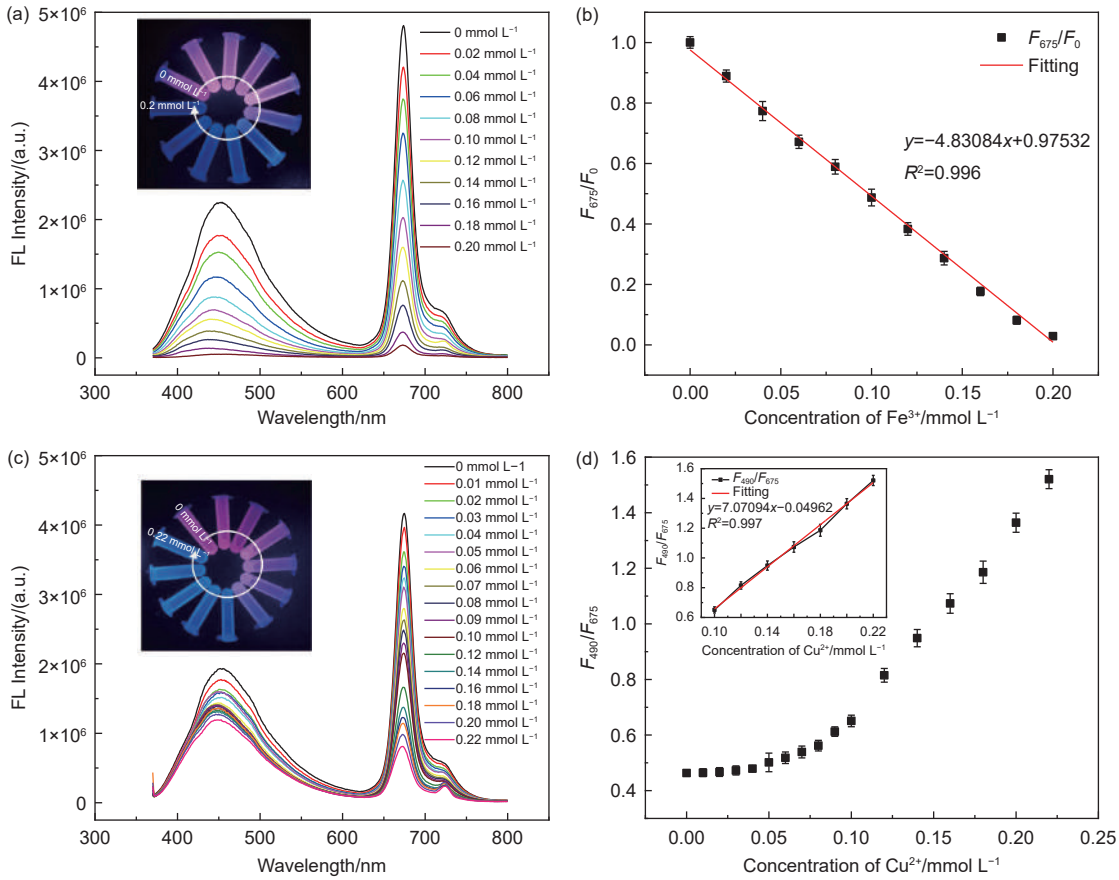

Fig. 9　(a) The influence of Fe^{3+} concentration on the fluorescence intensity of D-BCQDs3 (inset: fluorescence photographs of D-BCQDs3 after adding different Fe^{3+} concentrations under 365 nm UV light). (b) The linear relationship between F_{675}/F_0 and Fe^{3+} concentration. (c) The influence of Cu^{2+} concentration on the fluorescence intensity of D-BCQDs3 (inset: fluorescence photographs of D-BCQDs3 after adding different Cu^{2+} concentrations under 365 nm UV light). (d) The relationship between F_{490}/F_{675} and Cu^{2+} concentration (inset: the linear relationship between F_{490}/F_{675} and Cu^{2+} concentrations from 0.1 to 0.22 mmol L^{-1})

noting that the D-BCQDs synthesized in this work exhibited superior sensitivity for detecting Fe^{3+} and Cu^{2+} compared to previous studies (Table 2 and 3).

According to the results of the interference experiments illustrated in Fig. 10, the interference of other metal ions had a negligible effect on the fluorescence quenching, which indicated that D-BCQDs3 possessed excellent anti-interference properties.

It can be observed from Fig. 10 that the fluorescence of both 490 and 675 nm was completely quenched when Fe^{3+} and Cu^{2+} coexisted, making it impossible to distinguish them. However, when Fe^{3+} and Cu^{2+} were added to the D-BCQDs3 solution separately, Fig. 9a, c demonstrated that the decreases in fluorescence intensity at 490 nm were different. This indicated that the two quenching phenomena were not entirely identical. Taking advantage of this difference, different volume ratios of Fe^{3+} and Cu^{2+} were added to the D-BCQDs3 solution (the total concentration of Fe^{3+} and Cu^{2+} was 0.1 mmol L^{-1}). As shown in Fig. 11, there was a certain linear relationship between F_{490}/F_{675} and V_{Fe}^{3+}/V_{Cu}^{2+}, and we can effectively distinguish the ratio of Fe^{3+} to Cu^{2+} in a certain mixed solution using this linear relationship.

4.2 Possible detection mechanism of D-BCQDs

To obtain the possible mechanism of Fe^{3+} and Cu^{2+} detection, the UV-Vis absorption spectroscopy, fluorescence spectroscopy and fluorescence decay of D-BCQDs3 were performed.

As shown in Fig. 12a, the UV-vis absorption spectra of D-BCQDs3 did not change significantly after adding Fe^{3+}, and no new absorption peaks were produced, which indicated that there was no non-fluorescent ground state complex between them.

Table 2 Comparison of different BCQDs for detecting Fe^{3+}

Precursors	Methods	Emission peak/nm	Fluorescence color	LOD/μmol L^{-1}	Ref.
Phyllanthus acid	Hydrothermal	420	Blue	0.90	[48]
Poa pratensis	Hydrothermal	420	Blue	1.40	[49]
Sugarcane molasses	Hydrothermal	390	Blue	3.30	[50]
Rosehip	Hydrothermal	433	Blue	0.53	[51]
Cassava stem	Hydrothermal	440	Blue	0.91	[52]
Coffee waste	Hydrothermal	450	Blue	4.31	[53]
Viburnum awabuki leaves	Solvothermal	490 and 675	Purplish red	0.59	This work

Table 3 Comparison of different BCQDs for detecting Cu^{2+}

Precursors	Methods	Emission peak/nm	Fluorescence color	LOD/μmol L^{-1}	Ref.
Ganoderma lucidum bran	Hydrothermal	450	Blue	0.74	[54]
Radish	Hydrothermal	450	Blue	6.80	[55]
Acrocomia aculeate	Hydrothermal	452	Blue	0.99	[56]
Musa acuminata	Hydrothermal	420	Blue	1.65	[57]
Viburnum awabuki leaves	Solvothermal	490 and 675	Purplish red	0.41	This work

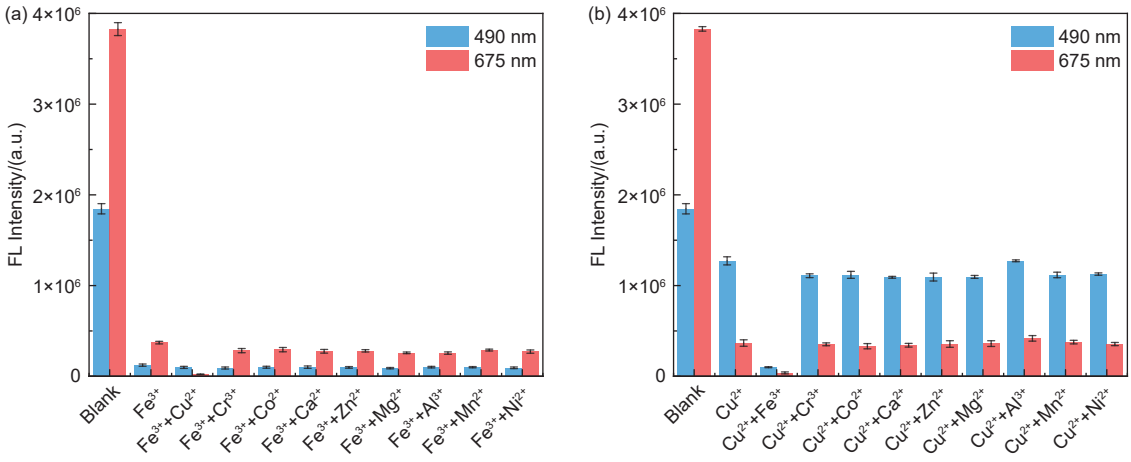

Fig. 10 Interference of other metal ions in detection of (a) Fe^{3+} and (b) Cu^{2+}

Fig. 12b depicted that there was some overlap between the UV-Vis absorption spectra of Fe^{3+} and the excitation spectra of D-BCQDs3, suggesting that fluorescence resonance energy transfer (FRET) or internal-filter effect (IFE) could be the detection mechanism[58]. However, one of the characteristics of the

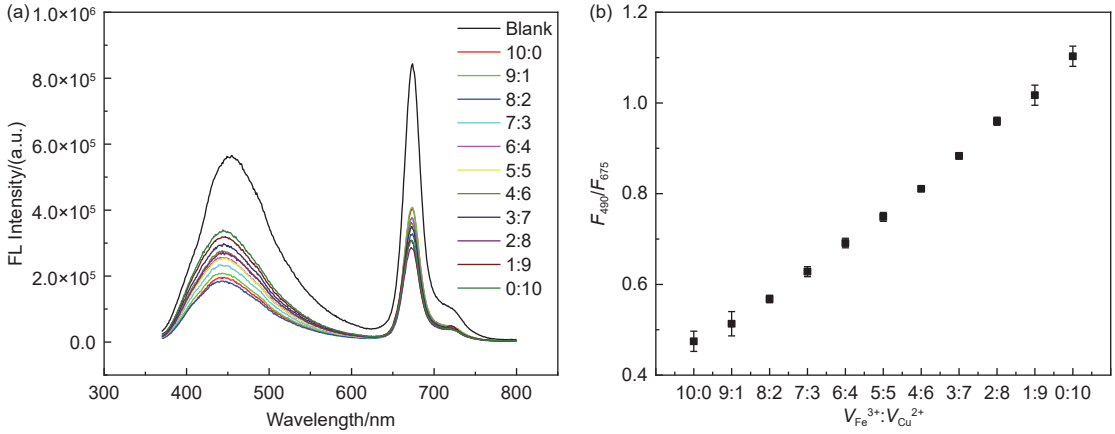

Fig. 11　(a) The influence of different volume ratios of Fe^{3+} to Cu^{2+} on the fluorescence intensity of D-BCQDs. (b) The relationship between F_{490}/F_{675} and V_{Fe}^{3+}/V_{Cu}^{2+}

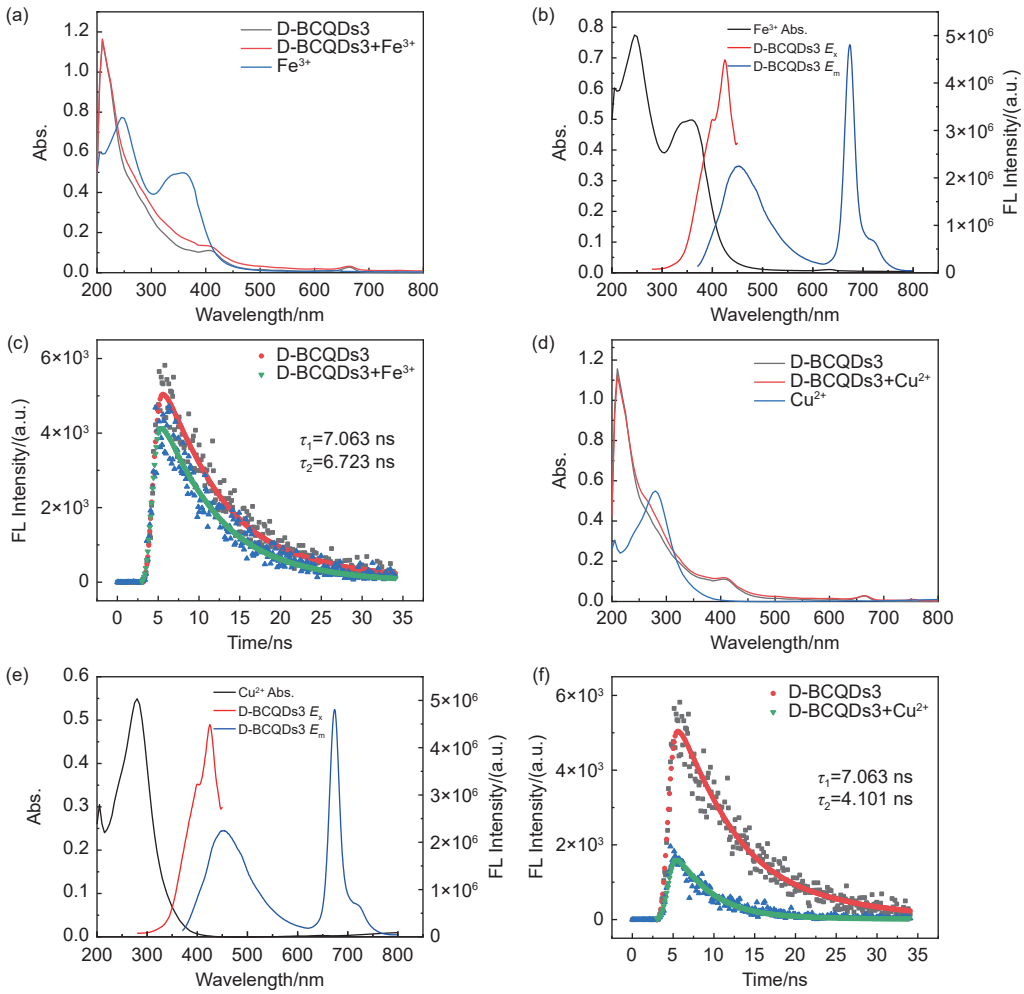

Fig. 12　(a) The changes of UV-vis absorption spectra of D-BCQDs3 after adding Fe^{3+}. (b) UV-Vis absorption spectra of Fe^{3+}, excitation and emission spectra of D-BCQDs3. (c) The changes of fluorescence lifetime of D-BCQDs3 after adding Fe^{3+}. (d) The changes of UV-vis absorption spectra of D-BCQDs3 after adding Cu^{2+}. (e) UV-Vis absorption of Cu^{2+}, excitation and emission spectra of D-BCQDs. (f) The changes of fluorescence lifetime of D-BCQDs3 after adding Cu^{2+}

FRET mechanism was the change in fluorescence lifetime[59]. There was no obvious variation in the fluorescence lifetime curves of D-BCQDs3 before and after adding Fe^{3+}, and the average fluorescence lifetimes were 7.063 and 6.723 ns, respectively (Fig. 12c). Therefore, it can be inferred that the detection mechanism of Fe^{3+} was IFE.

According to Fig. 12d, the absorption spectra of D-BCQDs3 showed no obvious change before and after Cu^{2+} was added, and there was some overlap between the excitation spectra of D-BCQDs3 and the UV-vis absorption spectra of Cu^{2+} (Fig. 12e). Moreover, it can be clearly seen from Fig. 12f that the fluorescence lifetime of D-BCQDs3 was shortened from 7.063 to 4.101 ns after adding Cu^{2+}. Therefore, we can conclude that the dynamic quenching process occurred between D-BCQDs3 and Cu^{2+}[60] by the FRET mechanism.

5 Conclusions

The fluorescence color tuning of D-BCQDs was achieved by a straightforward and eco-friendly solvothermal method based on temperature control. The fluorescence intensity at 490 nm strengthened primarily due to the increase in surface oxidation, while the decrease in nitrogen content led to a gradual reduction of fluorescence intensity at 675 nm. Moreover, the drop in the sp^2-C/sp^3-C hybridization domain ratio further confirmed the fluorescence color tunability of D-BCQDs. D-BCQDs showed excellent selectivity and sensitivity towards Fe^{3+} and Cu^{2+} detection and were able to quantify the ratio of Fe^{3+} to Cu^{2+} in a mixed solution. This work presented a simple method for preparing multicolor D-BCQDs and demonstrated the potential of D-BCQDs in selectively detecting multiple ions.

Conflicts of interest

There are no conflicts of interest to declare.

Acknowledgements

This work was supported by National Natural Science Foundation of China (52090033, 52090030).

References

[1] Zhang H, Kang S, Wang G, et al. Fluorescence determination of nitrite in water using prawn-shell derived nitrogen-doped carbon nanodots as fluorophores[J]. ACS Sensors, 2016, 1(7): 875-881.

[2] Yahaya Pudza M, Zainal Abidin Z, Abdul Rashid S, et al. Eco-friendly sustainable fluorescent carbon dots for the adsorption of heavy metal ions in aqueous environment[J]. Nanomaterials, 2020, 10(2): 315.

[3] Liang Y, Xu L, Tang K, et al. Nitrogen-doped carbon dots used as an "on-off-on" fluorescent sensor for Fe^{3+} and glutathione detection[J]. Dyes and Pigments, 2020, 178: 108358.

[4] Liu W, Zhang R, Kang Y, et al. Preparation of nitrogen-doped carbon dots with a high fluorescence quantum yield for the highly sensitive detection of Cu^{2+} ions, drawing anti-counterfeit patterns and imaging live cells[J]. New Carbon Materials, 2019, 34(4): 390-402.

[5] Quang N K, Hieu N N, Bao V V Q, et al. Hydrothermal synthesis of carbon nanodots from waste wine cork and their use in biocompatible fluorescence imaging[J]. New Carbon Materials, 2022, 37(3): 595-602.

[6] Yuan Y, Guo B, Hao L, et al. Doxorubicin-loaded environmentally friendly carbon dots as a novel drug delivery system for nucleus targeted cancer therapy[J]. Colloids and Surfaces B: Biointerfaces, 2017, 159: 349-359.

[7] Wang G, Guo Q, Chen D, et al. Facile and highly effective synthesis of controllable lattice sulfur-doped graphene quantum dots via hydrothermal treatment of durian[J]. ACS Applied Materials & Interfaces, 2018, 10(6): 5750-5759.

[8] Wang L, Weng S, Su S, et al. Progress on the luminescence mechanism and application of carbon quantum dots based on biomass synthesis[J]. RSC Advances, 2023, 13(28): 19173-19194.

[9] Zhu S, Meng Q, Wang L, et al. Highly photoluminescent carbon dots for multicolor patterning, sensors, and bioimaging[J]. Angewandte Chemie International Edition, 2013, 52(14): 3953-3957.

[10] Yan F, Jiang Y, Sun X, et al. Surface modification and chemical functionalization of carbon dots: A review[J]. Microchimica Acta, 2018, 185(9): 424.

[11] Li L P, Ren X F, Bai P R, et al. Near-infrared emission carbon dots for bio-imaging applications[J]. New Carbon Materials, 2021, 36(3): 632-638.

[12] Qu Y, Li D, Liu J, et al. Magnolia denudata leaf-derived near-infrared carbon dots as fluorescent nanoprobes for palladium(Ⅱ) detection and cell imaging[J]. Microchemical Journal, 2022, 178.

[13] Liu J, Geng Y, Li D, et al. Deep red emissive carbonized polymer dots with unprecedented narrow full width at half maximum[J]. Advanced Materials, 2020, 32(17): 1906641.

[14] Liu J, Kong T, Xiong H M. Mulberry-leaves-derived red-emissive carbon dots for feeding silkworms to produce brightly fluorescent silk[J]. Advanced Materials, 2022, 34(16): 2200152.

[15] Pak S J, Park J Y, Chung J W, et al. Color tunable carbon quantum dots from wasted paper by different solvents for anti-counterfeiting and fluorescent flexible film[J]. Chemical Engineering Journal, 2020, 383: 123200.

[16] Cheng C, Xing M, Wu Q. Preparation of carbon dots with long-wavelength and photoluminescence - tunable emission to achieve multicolor imaging in cells[J]. Optical Materials, 2019, 88: 353-358.

[17] Qin F, Bai J, Zhu Y, et al. Searching for the true origin of the red fluorescence of leaf-derived carbon dots[J]. Physical Chemistry Chemical Physics, 2023, 25(4): 2762-2769.

[18] Li J, Gong X. The emerging development of multicolor carbon dots[J]. Small, 2022, 18(51): 2205099.

[19] Torti S V, Torti F M. Iron and cancer: more ore to be mined[J]. Nature Reviews Cancer, 2013, 13(5): 342-355.

[20] Bao X, Cao X, Nie X, et al. A new selective fluorescent chemical sensor for Fe^{3+} based on rhodamine B and a 1, 4, 7, 10-tetraoxa-13-azacyclopentadecane conjugate and its imaging in living cells[J]. Sensors and Actuators B: Chemical, 2015, 208: 54-66.

[21] Park S H, Kwon N, Lee J H, et al. Synthetic ratiometric fluorescent probes for detection of ions[J]. Chemical Society Reviews, 2020, 49(1): 143-179.

[22] Fu Q, Zhou X, Wang M, et al. Nanozyme-based sensitive ratiometric fluorescence detection platform for glucose[J]. Analytica Chimica Acta, 2022, 1216: 339993.

[23] Liang Z, Zeng L, Cao X, et al. Sustainable carbon quantum dots from forestry and agricultural biomass with amplified photoluminescence by simple NH_4OH passivation[J]. Journal of Materials Chemistry C, 2014, 2(45): 9760-9766.

[24] Wang W, Li Y, Cheng L, et al. Water-soluble and phosphorus-containing carbon dots with strong green fluorescence for cell labeling[J]. Journal of Materials Chemistry B, 2014, 2(1): 46-48.

[25] Wang P, Yan Y, Zhang Y, et al. An Improved synthesis of water-soluble dual fluorescence emission carbon dots from holly leaves for accurate detection of mercury ions in living cells[J]. International Journal of Nanomedicine, 2021, Volume 16: 2045-2058.

[26] Wang Y, Lao S, Ding W, et al. A novel ratiometric fluorescent probe for detection of iron ions and zinc ions based on dual-emission carbon dots[J]. Sensors and Actuators B: Chemical, 2019, 284: 186-192.

[27] Yang Y Z, Xiao N, Cen Y Y, et al. Dual-emission ratiometric nanoprobe for visual detection of Cu(II) and intracellular fluorescence imaging[J]. Spectrochimica Acta Part A: Molecular and Biomolecular Spectroscopy, 2019, 223: 117300.

[28] Liang C, Xie X, Zhang D, et al. Biomass carbon dots derived from Wedelia trilobata for the direct detection of glutathione and their imaging application in living cells[J]. Journal of Materials Chemistry B, 2021, 9(28): 5670-5681.

[29] Pang S, Liu S. Dual-emission carbon dots for ratiometric detection of Fe^{3+} ions and acid phosphatase[J]. Analytica Chimica Acta, 2020, 1105: 155-161.

[30] Chen X P, Zhuang Y F, Lin J W, et al. Synthesis of N, S co-doped carbon dots for fluorescence detection of Fe^{3+} ions and intracellular pH imaging[J]. Chinese Journal of Analytical Chemistry, 2022, 50(11): 100151.

[31] Yang J, Ruan B, Ye Q, et al. Carbon dots-embedded zinc-based metal-organic framework as a dual-emitting platform for metal cation detection[J]. Microporous and Mesoporous Materials, 2022, 331: 111630.

[32] Zheng Y, Wan Y, Wei Y, et al. One-pot synthesis of dual-emissive carbon dots for ratiometric fluorescent determination of Hg^{2+}[J]. Journal of Fluorescence, 2023, 33(5): 1941-1948.

[33] Jia M, Peng L, Yang M, et al. Carbon dots with dual emission: A versatile sensing platform for rapid assay of Cr (VI)[J]. Carbon, 2021, 182: 42-50.

[34] Li L, Zhang R, Lu C, et al. In situ synthesis of NIR-light emitting carbon dots derived from spinach for bio-imaging applications[J]. Journal of Materials Chemistry B, 2017, 5(35): 7328-7334.

[35] Zhang T, Zhu J, Zhai Y, et al. A novel mechanism for red emission carbon dots: Hydrogen bond dominated molecular states emission[J]. Nanoscale, 2017, 9(35): 13042-13051.

[36] Zhu S, Song Y, Zhao X, et al. The photoluminescence mechanism in carbon dots (graphene quantum dots, carbon nanodots, and polymer dots): current state and future perspective[J]. Nano Research, 2015, 8(2): 355-381.

[37] Fang L Y, Zheng J T. Carbon quantum dots: Synthesis and correlation of luminescence behavior with microstructure[J]. New Carbon Materials, 2021, 36(3): 625-631.

[38] Wang L, Li W, Yin L, et al. Full-color fluorescent carbon quantum dots[J]. Science Advances, 6(40): eabb6772.

[39] Pan L, Sun S, Zhang L, et al. Near-infrared emissive carbon dots for two-photon fluorescence bioimaging[J]. Nanoscale, 2016, 8(39): 17350-17356.

[40] Ran Y, Wang S, Yin Q, et al. Green synthesis of fluorescent carbon dots using chloroplast dispersions as precursors and application for Fe^{3+} ion sensing[J]. Luminescence, 2020, 35(6): 870-876.

[41] Ma Y, Wu L, Ren X, et al. Toward kilogram-scale preparation of full-color carbon dots by simply stirring at room temperature in air[J]. Advanced Functional Materials, 2023, 2305867.

[42] Tetsuka H. Nitrogen-functionalized graphene quantum dots: A versatile platform for integrated optoelectronic devices[J]. The Chemical Record, 2020, 20(5): 429-439.

[43] Xu J, Liang Q, Li Z, et al. Rational synthesis of solid-state ultraviolet B emitting carbon dots via acetic acid-promoted fractions of sp^3 bonding strategy[J]. Advanced Materials, 2022, 34(17): 2200011.

[44] Li H, Han S, Lyu B, et al. Tunable light emission from carbon dots by controlling surface defects[J]. Chinese Chemical Letters, 2021, 32(9): 2887-2892.

[45] Yue J S, Yuan F Y, Qiu H X, et al. A review of fluorescent carbon dots: synthesis, photoluminescence mechanism, solid-state photoluminescence and applications in white light-emitting diodes[J]. New Carbon Materials, 2023, 38(3): 478-492.

[46] Wang B, Yu J, Sui L, et al. Rational design of multi-color-emissive carbon dots in a single reaction system by hydrothermal[J]. Advanced Science, 2021, 8(1): 2001453.

[47] Li B, Ma H, Zhang B, et al. Dually emitting carbon dots as fluorescent probes for ratiometric fluorescent sensing of pH values, mercury(II), chloride and Cr(VI) via different mechanisms[J]. Microchimica Acta, 2019, 186(6): 341.

[48] Atchudan R, Edison T N J I, Aseer K R, et al. Highly fluorescent

nitrogen-doped carbon dots derived from Phyllanthus acidus utilized as a fluorescent probe for label-free selective detection of Fe^{3+} ions, live cell imaging and fluorescent ink[J]. Biosensors and Bioelectronics, 2018, 99: 303-311.

[49] Krishnaiah P, Atchudan R, Perumal S, et al. Utilization of waste biomass of Poa pratensis for green synthesis of n-doped carbon dots and its application in detection of Mn^{2+} and Fe^{3+}[J]. Chemosphere, 2022, 286: 131764.

[50] Huang G, Chen X, Wang C, et al. Photoluminescent carbon dots derived from sugarcane molasses: synthesis, properties, and applications[J]. RSC Advances, 2017, 7(75): 47840-47847.

[51] Şenol A M, Bozkurt E. A green "off-on" fluorescent sensor to detect Fe^{3+} and ATP using synthesized carbon dots from Rosehip[J]. Research on Chemical Intermediates, 2023, 49(5): 2175-2189.

[52] Qiu Y, Li D, Li Y, et al. Green carbon quantum dots from sustainable lignocellulosic biomass and its application in the detection of Fe^{3+}[J]. Cellulose, 2022, 29(1): 367-378.

[53] Won S, Kim J. The detection of Fe (III) and ascorbic acid by fluorescence quenching and recovery of carbon dots prepared from coffee waste[J]. Korean Journal of Chemical Engineering, 2022, 39(10): 2826-2833.

[54] Wang B, Lan J, Ou J, et al. Ganoderma lucidum bran-derived blue-emissive and green-emissive carbon dots for detection of copper ions[J]. RSC Advances, 2023, 13(21): 14506-14516.

[55] Praneerad J, Thongsai N, Supchocksoonthorn P, et al. Multipurpose sensing applications of biocompatible radish-derived carbon dots as Cu^{2+} and acetic acid vapor sensors[J]. Spectrochimica Acta Part A: Molecular and Biomolecular Spectroscopy, 2019, 211: 59-70.

[56] Raja S, Da Silva G T S T, Anbu S, et al. Biomass-derived carbon quantum dot: "On-off-on" fluorescent sensor for rapid detection of multi-metal ions and green photocatalytic CO_2 reduction in water[J]. Biomass Conversion and Biorefinery, 2023, 14: 21925-21937.

[57] Chaudhary N, Gupta P K, Eremin S, et al. One-step green approach to synthesize highly fluorescent carbon quantum dots from banana juice for selective detection of copper ions[J]. Journal of Environmental Chemical Engineering, 2020, 8(3): 103720.

[58] Chen S, Yu Y L, Wang J H. Inner filter effect-based fluorescent sensing systems: A review[J]. Analytica Chimica Acta, 2018, 999: 13-26.

[59] Singh P, Arpita, Kumar S, et al. Assessment of biomass-derived carbon dots as highly sensitive and selective templates for the sensing of hazardous ions[J]. Nanoscale, 2013, 15(40): 16241-16267.

[60] Molaei M J. Principles, mechanisms and application of carbon quantum dots in sensors: A review[J]. Analytical Methods, 2020, 12(10): 1266-1287.